ADVANCED FUNCTIONAL MATERIALS
www.afm-journal.de

The Anisotropic Adsorption of De Novo Allosteric Two-Component Protein Fibers on Mica Surfaces

Chenyang Shi, Hao Shen, Yuna Bae, Jaeyoung Heo, Shuai Zhang, Lehan Yao, David Baker, and James J De Yoreo**

Protein adsorption at solid–liquid interfaces underlies many biomedical and materials applications, yet the mechanisms governing adsorption of proteins and their assemblies remain poorly understood. Here we investigate de novo–designed proteins that self-assemble into three fibrillar morphologies — small (S), large (L), and helical (H)—on muscovite mica. S-fibers are metastable, forming first but diminishing as L- and H-fibers develop and deposit. Adsorption of both fibers and monomers depends on fiber morphology and solvent environment, which is modulated by the substrate. The anisotropic surface features of the fiber types—long axis of S- and L-fibers and helical grooves of H-fibers—correlate with specific crystallographic directions on mica (001). S- and L-fibers align along the unique lattice axis, while the substrate-facing groove of H-fibers preferentially aligns along the remaining symmetry-related directions. Increasing potassium chloride (KCl) concentrations to molar levels alters adsorption, decreasing monomer coverage relative to fibers. These observations, interpreted through the effect of interfacial interface, indicate that ion-mediated modulation of hydration layers governs electrostatic interactions and alignment. This study reveals how coupling between protein topography, substrate crystallography, and hydration structure dictates selective adsorption and orientation of protein assemblies, offering insights for rational biomolecular material design.

1. Introduction

Proteins play a crucial role in a myriad of biological and technological processes, particularly at interfaces, where their adsorption and orientation significantly influence functionality.[1–6] Thus, understanding the controls on protein deposition at solid–liquid interfaces is important for applications ranging from biomaterials for implants and biosensors to drug delivery systems,[4,5,7–12] as well as efforts to design and synthesize hierarchically organized materials that take advantage of the high information content that proteins provide.[13–17] A significant number of interactions between functional groups on proteins and surfaces, such as cell membranes,[11,18] impact protein adsorption. However, the complexity of protein behavior at interfaces poses a considerable challenge due to the interplay of these surface chemical controls with other factors, including topography and the interaction of both proteins and surfaces with the surrounding aqueous environment.[14,19,20] Deeper insight into the interplay of these factors is expected to provide a framework for advancing the above applications.

Numerous systems of proteins and solid surface systems have been developed, with many proteins assembled through epitaxial relationships with the underlying mineral surfaces.[13–17,21–26] In the case of mica surfaces, recent studies have shown that proteins designed de novo to interact in an epitaxial manner can assemble into ordered patterns that reflect interactions beyond the simple epitaxial relationship encoded into the protein sequence.[15,27,28] Computational studies have shown that directional interactions of proteins

C. Shi, Y. Bae, J. Heo, S. Zhang, L. Yao, J. J De Yoreo
Physical Sciences Division
Pacific Northwest National Laboratory
Richland, WA 99354, USA
E-mail: james.deyoreo@pnnl.gov

H. Shen, D. Baker
Department of Biochemistry
University of Washington
Seattle, WA 98105, USA
E-mail: dabaker@uw.edu

H. Shen, D. Baker
Institute for Protein Design
University of Washington
Seattle, WA 98105, USA

S. Zhang, J. J De Yoreo
Department of Materials Science and Engineering
University of Washington
Seattle, WA 98105, USA

D. Baker
Howard Hughes Medical Institute
University of Washington
Seattle, WA 98105, USA

The ORCID identification number(s) for the author(s) of this article can be found under https://doi.org/10.1002/adfm.202520864

DOI: 10.1002/adfm.202520864

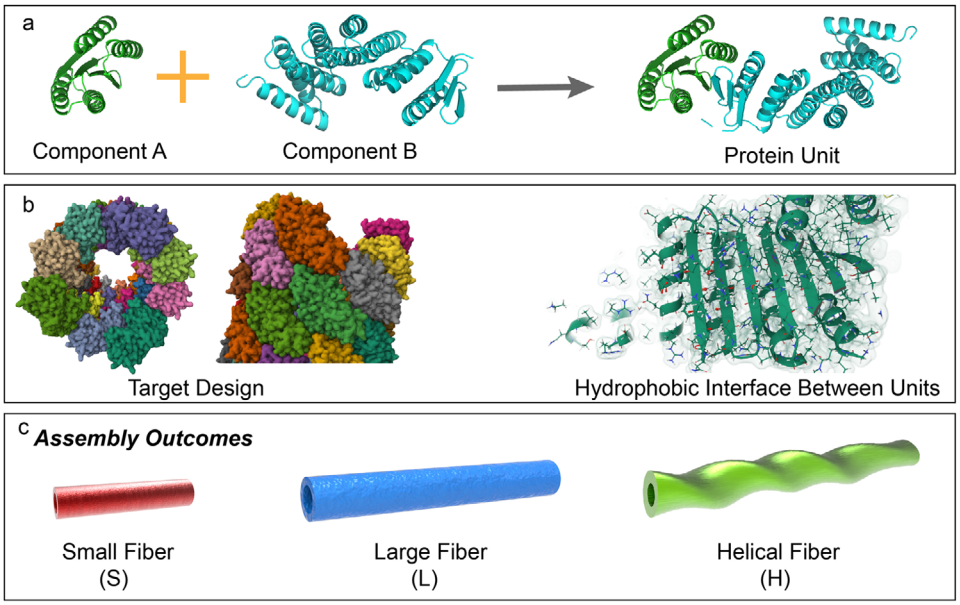

Figure 1. Design of two-component protein fibers. a) The images show the designed components A and B, as well as the resulting reconfigurable heterodimer scaffold unit (A+B) derived from Rosetta modeling. b) left: the model displays the predicted compact packing arrangement of the fiber subunits based on the sequence design, and the right panel shows the hydrophobic interface between components A and B, mainly arising from the β-sheet-forming regions. c) Schematic of observed morphologies. The morphology is governed by the amino-acid sequence; omission of the Leu residues in component B results predominantly in L-fiber formation.

with these surfaces reflect the manner in which solution conditions, such as ionic strength and electrolyte type, influence the aqueous response to both the mica surface and approaching proteins across different length scales.[14,29,30]

While the above line of research has focused on the influence of interfacial properties and protein binding to mineral surfaces on the resulting assembly of proteins into larger length scale 2D surface phases, the ability of the surface to select for adsorption of diverse pre-assembled protein structures has not been explored. In this work, we investigate the adsorption onto mica surfaces by de novo designed proteins that assemble into fibers through hydrophobic interactions between two distinct components (**Figure 1**). Our observations show that these two components assemble into three fibrillar architectures that include small (S), large (L), and helical (H) fibers, each characterized by a unique energy landscape of adsorption in aqueous environments. We further demonstrate that the deposition behaviors of these protein assemblies on mineral surfaces are strongly influenced by the potassium ion concentration, which is modulated by the structural properties of the mineral interface. In addition, we find that the orientational dependence of the adsorption energy landscape is dependent on fiber-type: the S and L fibers adsorb to the mica substrate along one preferential direction of the K^+ sublattice, which corresponds to the unique axis of muscovite mica, while the orientation of the H fiber is defined by the coalignment of the substrate-facing groove of the fiber helix with the other two symmetry equivalent directions of the K^+ sublattice. The results highlight the importance of the interplay among the details of the solution response and protein binding to solid surfaces, providing fundamental insights into the controls on protein adsorption.

2. Results

2.1. Protein Design

Protein fibers were formed through the co-assembly of two distinct components. Components A and B are rationally designed heterodimers and heterotrimers, composed of monomeric subunits shaped as helical hairpins (Figure 1a). These subunits interact through buried hydrogen bond networks that impart high binding specificity. Component A features four α-helices coupled with β-sheet elements, while component B is larger in size, consisting of ten α-helices and presenting exposed β-sheets at its boundary. Upon mixing, each subunit is designed to selectively pair with its designated partner through a hydrophobic interface to form a tubular filament[31] (Figure 1b).

2.2. The Morphology and Assembly of the Protein Fiber

Using atomic force microscopy (AFM), which is a versatile method for investigating biomolecules and their assemblies on surfaces,[32,33] we characterized the structures formed upon mixing of the two protein components. Results on solutions deposited on muscovite (M-) mica show that, contrary to the intended design, the proteins assemble into three distinct architectures: S-fibers, L-fibers, and H-fibers (**Figure 2**a–g). The respective heights of the fibers are ≈10, ≈18, and ≈21 nm (Figure 2k–m), with the diameter of the L-fibers being equal to that of the intended design. Both the S- and L-fibers display a smooth, homogeneous outer surface, whereas the H-fiber exhibits a right-handed helical twist with a 70 nm pitch, as seen by the 30° groove angle (Figure 2e–g; Figure S1, Supporting

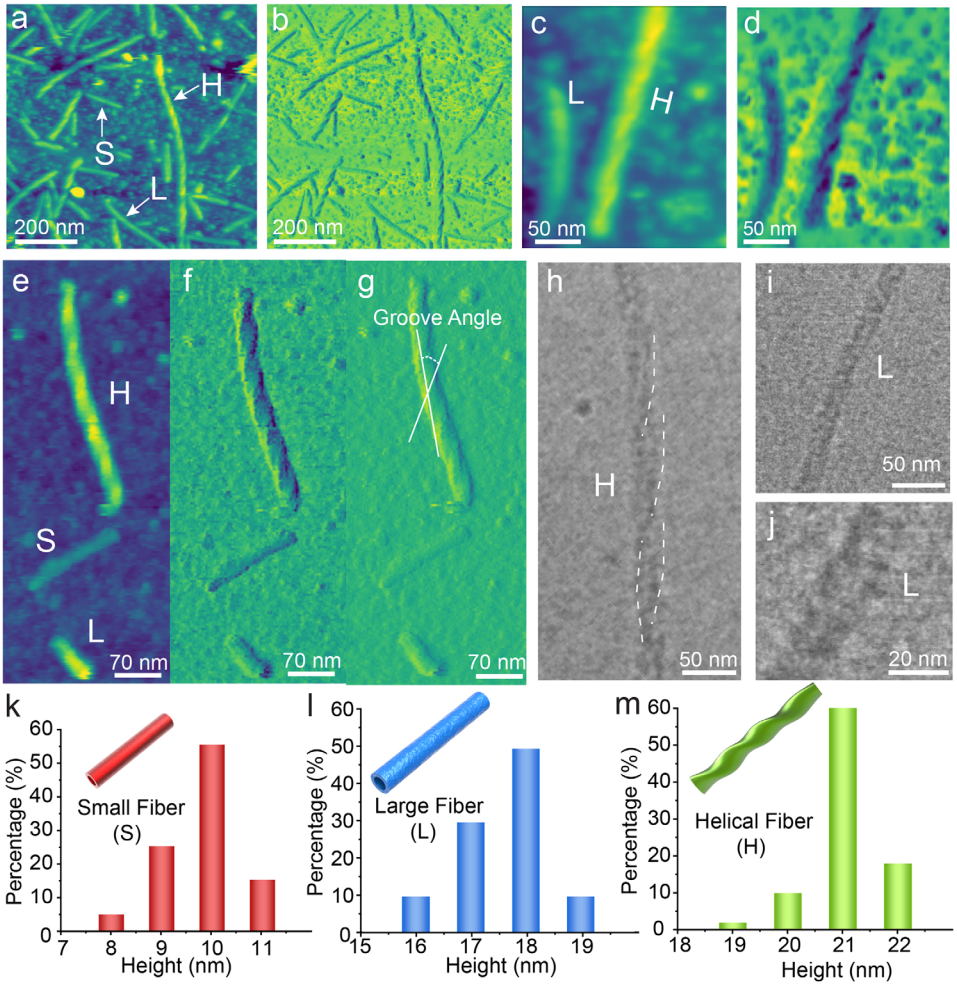

Figure 2. The structure of de novo protein fibers. a,b) AFM topography (a) and phase (b) images of protein fibers deposited on M-mica surfaces. The letters S, L, and H denote small, large, and helical fibers, respectively. c,d) Higher resolution AFM images of L- and H-fibers: (c) topography, (d) phase. e–g) AFM images of the various fibers: (e) topography, (f) phase, and (g) amplitude. h–j) Cryo-EM images of protein fibers: (h) H-fiber, (i, j) L-fiber. k–m) Height distribution profiles for the three types of protein fibers (S, L, and H), sample size >30. AFM and Cryo-EM images captured in 0.4 M KCl solution.

Information). The S-fiber can reach lengths of up to 250 nm, whereas the H- and L-fibers can extend to several micrometers (Figures S1 and S2, Supporting Information). Cryo-EM images of the H- (Figure 2h) and L-fibers (Figure 2i–j) are consistent with the AFM results, demonstrating that the protein fibers maintain their morphology when adsorbing from the bulk solution to the mica surface and that, in particular, the helical morphology of the H-fibers is not a consequence of the protein-surface interaction. Moreover, despite their distinct morphologies, the formation of all three fiber types requires interactions between both protein components; no fibers form in separate solutions of components A or B, even after prolonged incubation times (Figure S3, Supporting Information).

Analysis of AFM images collected at different timepoints (**Figure** 3a,b) indicates fiber formation follows a multistage process in which: i) a minimum incubation time is required for the formation of all fiber types and, thus, no fibers are observed upon introduction of the protein solution; instead, only protein monomers are observed. ii) By 10 h, S-fibers appear, but L- and H-fibers require longer incubation periods, appearing only after 48 h. iii) H-fiber assembly progresses slightly faster than does L-fiber assembly in the early stages, with H-fibers measuring ≈300 nm in length and containing 4–5 helical turns. iv) The number of S-fibers initially increases, as do their lengths, but later they cease to grow and their number declines, showing that they dissociate as the larger fibers begin to dominate and continue to elongate. For example, by 90 h H and L fibers reach ≈500 nm in length, whereas S fibers remain under 250 nm (Figure 3a–90h and S4, Supporting Information).

Considering the principles underlying classical nucleation theory,[34,35] the above results imply a dependence of the work of fiber formation ΔG on the progress of protein fiber assembly in which S-fibers possess a lower free energy barrier ΔG^* to nucleation, facilitating faster initial assembly, but they have lower thermodynamic stability (i.e., higher solubility) as compared to L and H-fibers, leading to their eventual replacement by the larger structures, leading to a crossover in the magnitude of ΔG (Figure 3c). Thus, S fibers are metastable and provide

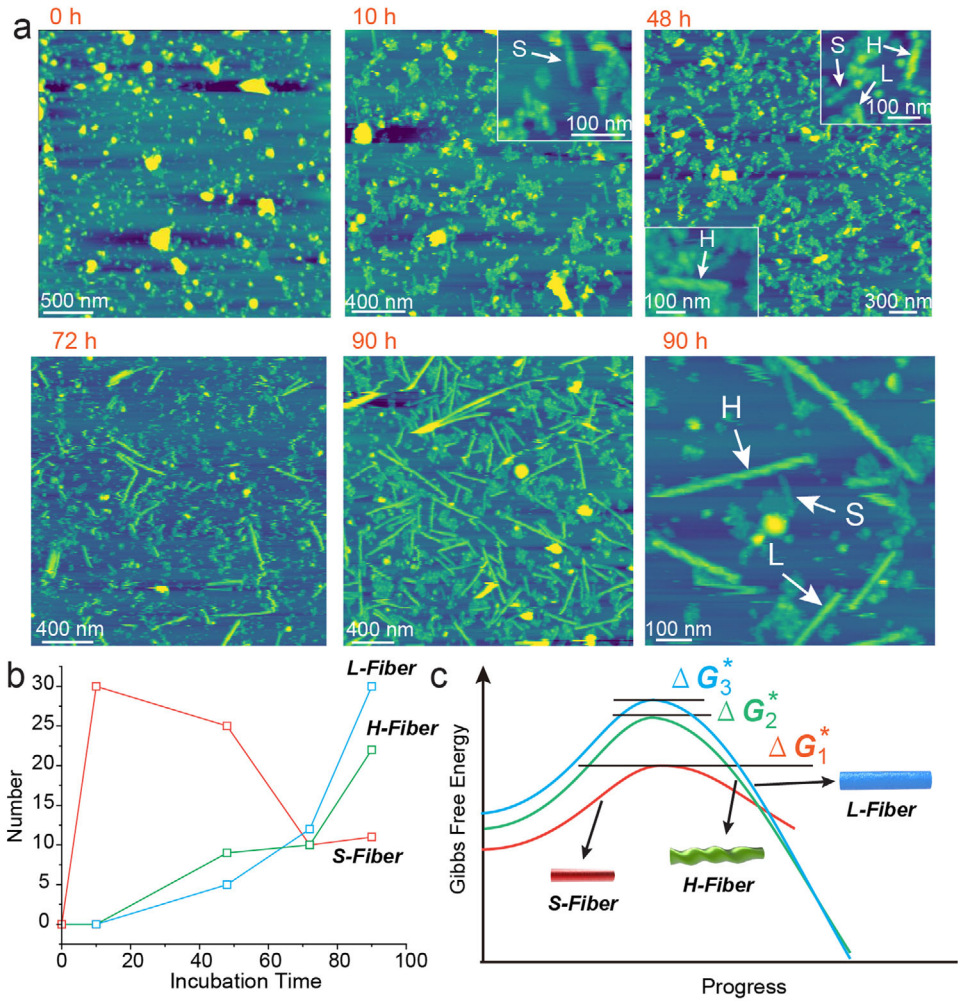

Figure 3. De novo protein fiber assembly. a) AFM topography of 1 μM protein samples deposited on M-mica at various growth times (0–90 h). AFM images captured in 1 M KCl solution, see details in the experimental section. b) The number of distinct types of protein fibers as a function of incubation time (hour), measured over an area of 4 μm^2. c) Schematic showing the work of formation (i.e., the Gibbs free energy vs progress) for the three types of protein fibers where ΔG_1, ΔG_2, and ΔG_3 correspond to the S-, H-, and L-fibers, respectively. Schematic representation of the qualitative free energy landscape of fiber assembly. The relative barrier heights illustrate the nucleation energy barriers for the formation of different fiber types.

another example of biomolecular systems that exhibit metastable precursors during assembly[36–38] and an illustration of Ostwald's Rule of Stages, which is an empirical rule stating that less stable phases appear first and are sequentially replaced by the more stable phases in order of increasing stability.[39,40] Given that the L- and H-fibers maintain similar populations and each grows until the end of the experiment, they must have similar free energies of formation, though because the H-fibers appear and build in number more quickly than the L-fibers, they likely have the lower value of ΔG^*.

2.3. The Deposition Behavior of the Protein Fiber

The observed deposition behavior of protein solutions on M-mica surfaces varies with salt concentration. At 0.04 M KCl (**Figure** 4a), deposition of a 1 μM protein solution on M-mica results in a surface that is densely covered with protein monomers but exhibits minimal fiber formation.

As the KCl concentration increases to 0.4 M (Figure 4b), the number of protein fibers rises while the surface remains largely coated with smaller protein units. At 1 M KCl (Figure 4c), fiber structures dominate, with protein monomers nearly absent. Statistical analysis (Figures S5 and S6, Supporting Information) reveals a significant increase in both the number and length of adsorbed protein fibers at the higher KCl concentration. The deposition count for S-fibers increases tenfold, though their length still remains short. In contrast, L- and H-fibers exhibit substantial elongation, indicating that high KCl concentrations either increase the rate of elongation in the bulk solution or lower the deposition barrier for longer fibers. However, at concentrations exceeding 3 M KCl, both protein monomer and fiber deposition are inhibited, leading to regions devoid of adsorbed proteins (Figure 4d). Moreover, many of the fibers that are observed are entangled with others, indicating that high salt leads to fiber aggregation in solution.

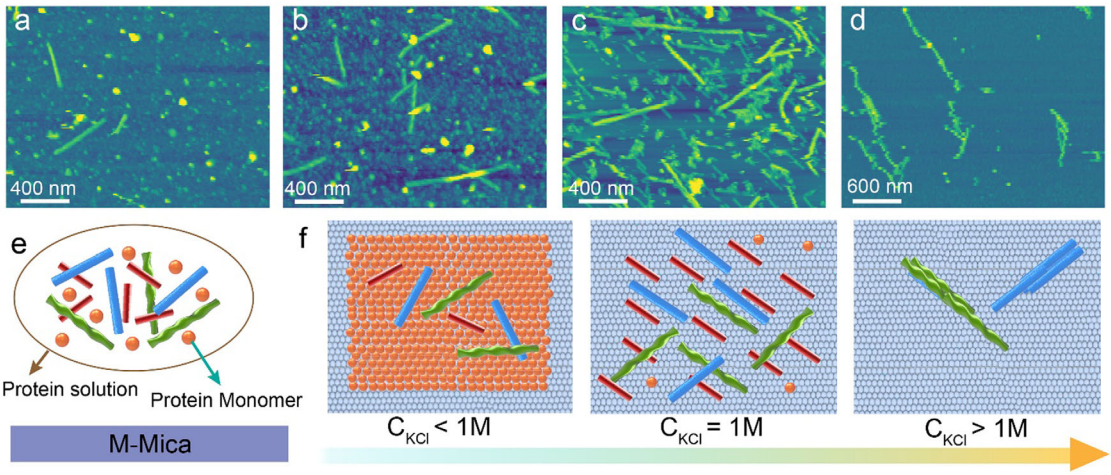

Figure 4. Adhesion of De Novo Protein Fibers on Muscovite Mica. a–d) AFM topography images of 1 μM protein samples in KCl solutions with varying concentrations: (a) 0.04 M, (b) 0.4 M. (c) 1 M, and (d) 3 M. e) Schematic representation of components present in the protein solution. f) Schematic illustration showing the adhesion behavior of protein fibers and their constituent units.

When NaCl is used instead of KCl, protein fibers fail to deposit efficiently on mica, even at 1 M NaCl (Figure S7, Supporting Information), highlighting the importance of electrolyte species in controlling fiber adsorption. Our results show that distinct deposition behaviors occur across different KCl concentrations, influencing both the ratio of deposited protein fibers and their average length (Figure 4e,f).

To further examine the influence of solid surface, we investigated deposition on another type of mica: fluorophlogopite (F-mica). The primary differences between the M-mica and F-mica structures are restricted to their subsurface layers: F-mica contains a complete Mg^{2+}-F network below the tetrahedrally coordinated aluminosilicate surface layer, while, in M-mica, this layer has vacancies in which Al^{3+}-coordinated OH groups sit and point toward the surface along two of the three lattice vectors that define the three-fold symmetric lattice of surface-exposed K^+ ions.[14,30] Our results show that the adsorption behavior of the proteins is different on M- and F-mica. At 1 M KCl, protein monomers still cover the F-mica surface (**Figure 5**a), however a deposition pattern similar to that observed on M-mica at 1 M KCl emerges on F-mica only at KCl concentrations >1.5 M (Figure 5b), suggesting that a higher KCl concentration is required to inhibit protein monomer and promote protein fiber adsorption.

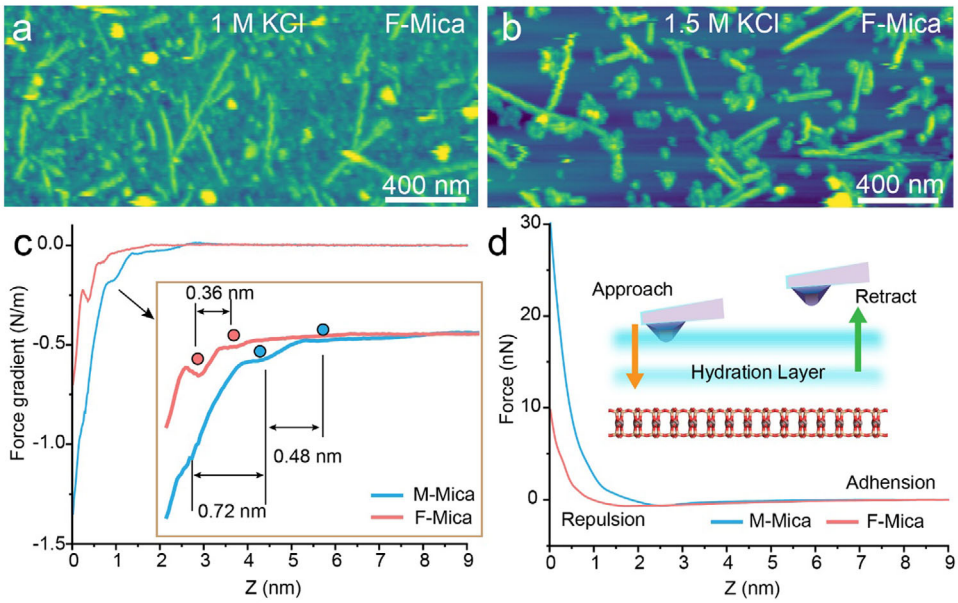

Figure 5. Surface Deposition on F-Mica and comparison of force profiles for the F- and M-mica. a–d) AFM topography images of 1 μM protein samples in KCl solutions on F-mica at varying concentrations (1 and 1.5 M). (c) Average force gradient curves obtained on M-Mica (cyan color) and F-Mica (pink color) in 1 M KCl. (d) Force–distance curves recorded on different mica surfaces, with each curve averaged over 200 samples.

To examine the importance of hydrophobic interactions in adsorption and assembly, we investigated adsorption and assembly on a typical hydrophobic surface, namely that of highly ordered pyrolytic graphite (HOPG), which results in very different behavior than seen on mica. Even at 2 M KCl, protein monomers remain firmly adsorbed with minimal fiber formation (Figure S8, Supporting Information). From this, we conclude that the hydrophobic interaction between HOPG and the hydrophobic pockets on the monomers that normally drive assembly into fibers, at which time they are no longer exposed, becomes so strong that monomers adsorb to the HOPG before assembly is able to occur. This observation shows that protein adsorption is influenced by both the solution environment and the substrate properties, with hydrophobic surfaces favoring monomer adsorption rather than assemblies.

To obtain a better understanding of the differences in protein adsorption on different mica substrates, we employed Fast Force Mapping Mode (FFM), an AFM technique in which a nanoprobe navigates the interfacial region and records force variations corresponding to solution structuring.[41–44] Plots of the average force gradient vs height (Figure 5c) show that the distance between the first and second hydration, and hydration layer spacings were determined from >200 independent force curves for each substrate (Figure S9, Supporting Information). The mean spacing was 0.36 ± 0.03 nm for F-mica and 0.48 ± 0.03 nm for M-mica, where the error represents the standard deviation. The near-surface oscillatory component, attributed to hydration structure, is superimposed on a long-range repulsive component,[30] which is distinctly larger for M-mica, as seen through the more rapid decrease in force gradient with distance. This increased repulsive force may arise from site-specific chemical interactions or reduced tip-substrate separation.[30]

The above results show that, at higher salt concentrations (≈1M), the nature of the protein adsorption undergoes a transition: at low KCl concentration (0.04 – 0.4 M), protein monomers reach the surface, but as salt concentration increases to 1M or more, only larger protein assemblies are deposited. This suggests that the interfacial solution structure at high salt concentrations acts as a barrier to protein monomer adsorption while facilitating protein fiber deposition or, at least, not inhibiting it. Comparing M-mica to F-mica, a greater number of protein monomers adsorb on F-mica, indicating that the interfacial structure of M-mica imposes a stronger adsorption barrier. This conclusion is supported by the measurements of a larger repulsive hydration force on M-mica than F-mica (Figure 5d).

2.4. The Orientation Behavior of the Protein Fiber

Protein fiber assemblies adsorb onto the mica surface with preferred orientations (**Figure 6**a–c). The S-fibers adsorb with their long axis aligned almost exclusively with one of the close-packed directions the K^+ sublattice of M-mica (001) (Figure 6c), which are offset by 60° intervals (Figure 6f and Figure S10, Supporting Information),[14,45] implying that this is the minimum energy configuration for this fiber-type. Given that, as discussed above, two of the three directions of the K^+ sublattice on M-mica (001) are crystallographically identical and only the third is distinct, this orientation must be the unique direction of the lattice. For the purposes of comparison with the other fiber types, we denote this orientation as lying at an angle of 0°. Most L-fibers adopt this same orientation but show a broader angular distribution. In contrast, H-fibers display a distinct asymmetry that is tied to the helical nature of the fibers. In most cases, the top groove of the helix aligns with the S-fiber direction (white boxes in Figure 6c). Defining β as the angle between the H fiber's axis and the S-fiber direction, and θ as the helical pitch angle (top groove and bottom groove, Figure 6d,e), the groove facing the substrate (bottom groove, Figure 6d) forms an angle $\alpha = \beta + \theta$ relative to the S fiber. In Figure 6d,e,h, β is the same as θ, because the top groove matches the S-fiber direction (white boxes in Figure 6c). With β and θ each ranging from 30° to 60° (Figure 6e,g), the resulting value of α spans 60°–120°, thus generally aligning the bottom groove with the remaining mica symmetry axes. Thus, there is a symmetry-based partitioning of the H-fiber direction driven by its intrinsic helicity and chirality.

To further understand how the alignment of the H-fibers arises, we performed in situ AFM imaging to capture the dynamics of adsorption and growth on M-mica in 1 M KCl solution (**Figure 7**a–l). During the assembly process, newly formed helical turns were clearly resolved along the H-fiber surface. Figure 7n shows that the newly formed turns each maintained the existing (and uniform) helical pitch of the H-fibers. A magnified top-view image (Figure 7m) reveals that the pitch of the newly formed turn closely matches that of the S-fiber alignment, which is known to preferentially follow the unique symmetry axis of mica (100). Notably, since the helical groove of the H-fiber forms at 30° angle relative to the fiber axis (Figure 7o), this observation implies that the substrate-facing groove direction of the H-fiber is rotated ≈60° (or 120°) from the S-fiber axis. This angular offset corresponds precisely to the remaining symmetry directions of the mica lattice, thereby explaining the observed deviation in the overall alignment of H-fiber axes compared to the S-fibers. These data provide direct structural evidence linking the helical pitch geometry to substrate-specific orientation of adsorption.

3. Discussion

The results presented above show that the adsorption of the protein fibers on the mica surface in aqueous salt solution depends on the structure of the substrate, the electrolyte concentration and electrolyte type, and the nature of the protein species (i.e., monomers, or S-, L or H-fibers). In this study, the fact that the protein fibers exhibit the same structures whether in bulk solution or on the surface, eliminates the influence of secondary structural evolution or 3D conformational changes induced by the interfacial solution environment or substrate during adsorption as a source of the observed differences. On the other hand, previous investigations of the mica surface in electrolyte solutions and the interaction of proteins with the surface showed that all of these factors impact the response of the interfacial hydration environment and, hence, the forces and energy landscape experienced by protein species as they approach and adsorb to the surface[14,29,30,46,47]. Thus, understanding how the hydration environment, which is altered by the surface, impacts the protein-substrate interactions becomes central to unraveling the protein adsorption behavior.

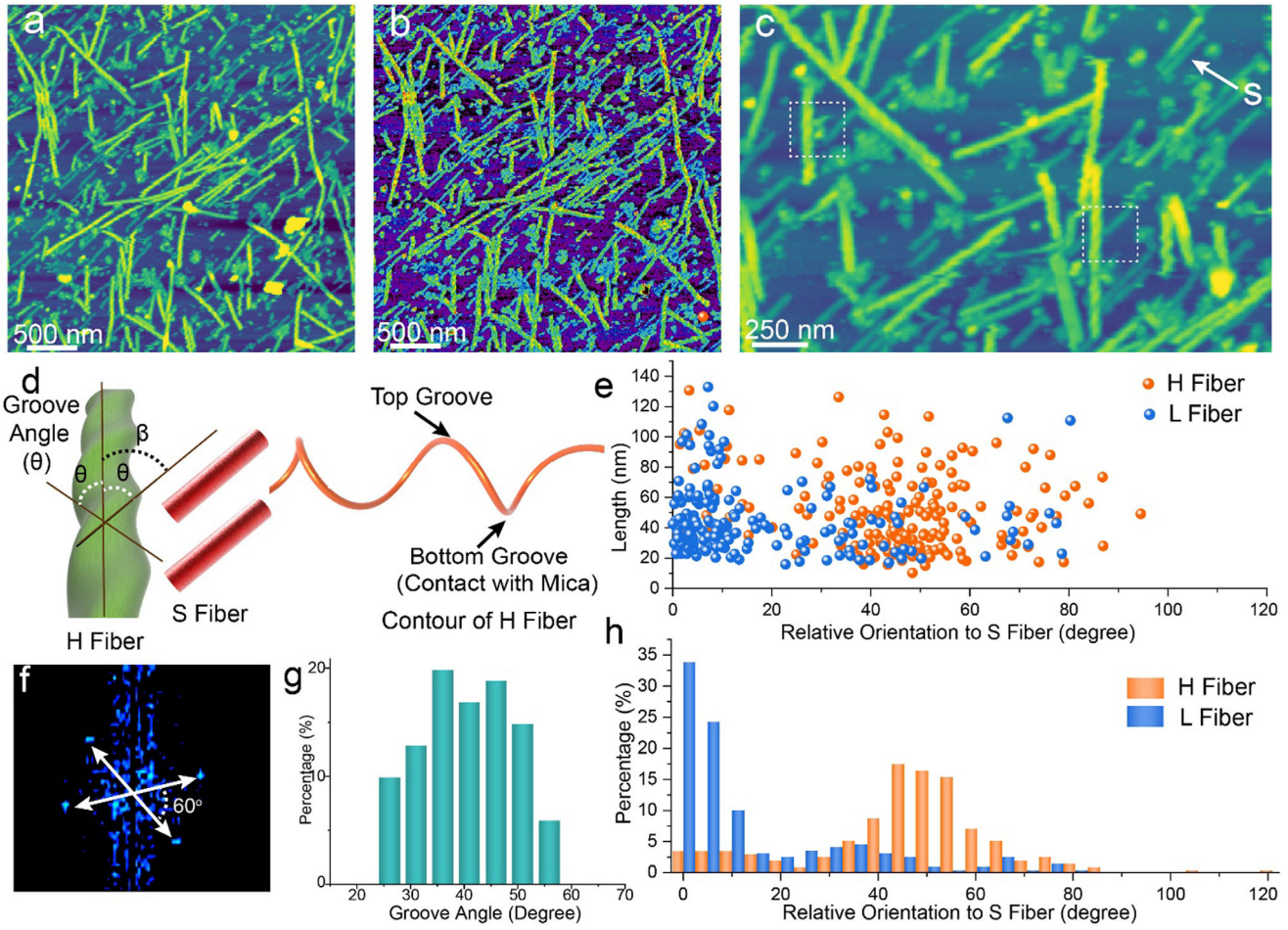

Figure 6. Orientations of Fibers on Mica Surfaces. a,b) AFM topography image (a) and phase image (b) of 1 μM protein samples in 1 M KCl solution on M-mica. c) Magnified AFM image highlighting the orientation of protein fibers on the mica surface. The white dashed boxes highlight S fibers that are aligned with a top-facing groove of the fiber, and the white arrow points to an isolated S fiber. d) The simplified model and contour of H fiber to show the groove angle of H-fiber on the substrate. Grooves on the bottom are at an angle $\alpha = \beta + \theta$ relative to the S fiber. e) The statistical data analysis to depict the orientation fluctuations of H and L- fibers relative to the S-fiber. f) FFT data of the mica surface collected in the protein solution. g) The distribution of groove angle on H-fiber. h) The histogram analysis to show the orientation fluctuations of H and L- fibers relative to the S-fiber.

Previous studies also demonstrated that adsorption of various proteins on mica in KCl solutions follows a concentration-dependent transition from isolated monomers to organized assemblies and suggested that proteins interact with the interfacial solvent near the surface and not just directly with the potassium ions in the surface lattice[14,17,30]. Our findings reveal an even more intricate behavior: as K^+ concentration increases, the adsorption of protein monomers rises, whereas that for protein fibers decreases. This opposing trend also suggests that protein adsorption is governed by the interfacial solvent layer rather than just direct interactions with potassium ions.

In fact, a number of studies of ion-specific effects at the mica surface have shown that Na^+ and K^+ affect the hydration structure differently: Na^+ is more strongly hydrated and reinforces the ordered interfacial water layers, whereas K^+ sits tightly in the ditrigonal cavities coordinated with the surrounding basal oxygens and weakens this hydration structure[43,48–50]. Moreover, switching from K^+ to Na^+ flips the long-range electrostatic interactions with negatively charged proteins from attractive to repulsive due to changes in the interfacial water structure[14,29,30,46,47]. These ion-specific differences in hydration structure and the nature of water-surface interactions may provide an explanation for why monomers and fibers exhibit the opposite trends in adsorption at the same salt concentration when KCl is switched to NaCl: Protein monomers have exposed hydrophobic sidechains, whereas these non-polar residues are buried in the fibers. Thus, monomers and fibers respond differently when the hydration structure is altered by this switch.

If protein adsorption were directly governed by K^+, both the protein monomers and the fibers should exhibit the same trend in adsorption with increasing K^+ concentrations. However, they exhibit opposite trends. Our results do not enable us to conclude the reason for these reversed trends. Nonetheless, we can speculate as to why this behavior is manifest. If this is a purely kinetic effect, then it may be that the repulsive forces prevent the approach of monomers due to exposed sidechains that interact with the ion-solvent network that develops at high salt

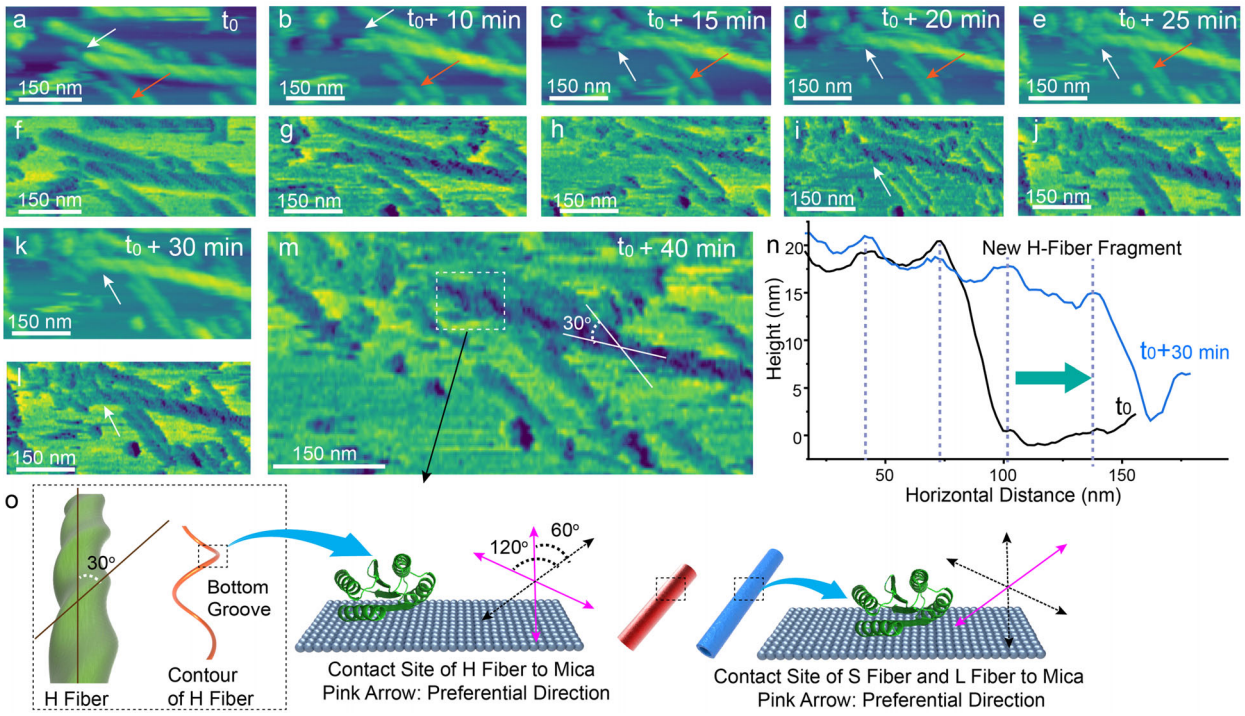

Figure 7. In situ AFM observation of H-fiber assembly on M-mica. a–e,k) Time-resolved AFM topography images showing the assembly of H-fibers in 1 M KCl solution on M-mica. f–j,l) Corresponding phase images for panels a–e and k, respectively. The white arrows in panels a–i point to the tip positions of H fibers, highlighting the regions of new growth, clearly showing the pitch of the fiber. m) Magnified topography image highlighting the orientation of the newly formed helical pitch on assembled H-fibers. n) Height profile along the white line in panel k, revealing the periodic pitch structure of the H-fiber. o) Structural models depicting the angle between the fiber's local surface topography and the mica substrate at the solid–liquid interface. The pink arrows point to the preferential orientation angle.

concentration[43], while the burial of such residues within the assembled fibers eliminates this barrier to adsorption. If, instead, it is a thermodynamic outcome reflecting a lower binding energy for monomers and/or a higher binding energy for fibers at high K^+ concentration, it may be that the residues that are responsible for protein monomer binding to the surface interact with the ditrigonal cavities of the mica surface where the K^+ ions sit. Consequently, at high KCl concentration, the filling of these cavities eliminates the sites of strong adsorption for the proteins. Whatever the reason, these findings underscore the complex interplay between protein monomer, assembled structures, and mineral surfaces in regulating the interfacial environment that governs adsorption.

Previous studies have shown that numerous proteins assemble on M-mica surfaces with an alignment that is either along the single unique symmetry axis or along the other two symmetry axes, but not all three, despite the inherent three-fold symmetry of the K^+ sublattice itself.[15,17,30,47,51,52] This preferential alignment has been attributed to the influence of interfacial hydration structure. Specifically, while the first hydration layer on the mica surface exhibits the three-fold symmetry of the underlying surface lattice, the asymmetry of the underlying layer causes the dipoles of the water molecules in the first layer to become aligned along a single direction, which in turn causes the water molecules of the second hydration layer to partition into stripes that align along the unique axis.[30] These oriented water molecules create an asymmetric energy landscape that may be responsible for guiding protein alignment either along the single symmetry axis or the other two symmetry axes.[15]

While these previous studies provide a framework for understanding the alignment of S- and L- fibers along the unique axis of the M-mica (001) surface, the H-fiber assemblies display distinct behavior (Figure 7o); the fiber axis deviates from both the unique and the two symmetry-equivalent axes, Instead, our results show that the bottom groove of the helix aligns with the two remaining symmetry axes. Why the preferential direction of the groove is along these two axes rather than the unique axis cannot be determined from our results or from the previous studies of the water-mica interface, but this decoupling of fiber axis from groove orientation underscores the complex interplay between molecular geometry, interfacial hydration, and lattice symmetry in directing protein adsorption behavior.

It is worth noting that while the present study focuses on monovalent salts (NaCl and KCl) to minimize bulk aggregation effects, divalent cations such as Ca^{2+} and Mg^{2+} are expected to further modulate hydration structure and interfacial assembly through stronger electrostatic screening and site-specific coordination. This aspect is currently under investigation using a related protein system.

4. Experimental Section

Material: The computational design and protein expression/purification workflow[31,53] was applied to multi-component proteins to

generate models of helical filament architectures. Synthetic genes were optimized for expression in Escherichia coli and synthesized by genscript and IDT. Protein expression was induced using the Studier autoinduction method[54] at 37 °C for 24 h. Following induction, cells were harvested by centrifugation, resuspended in Tris-buffered saline (TBS), and lysed with BugBuster detergent. Protein monomers (Components A and B) were mixed at a 1:1 mass ratio and incubated for over 10 h to promote the formation of protein assemblies.

Computational Design Approach: The helical docking and design methodology[53] was applied to two-component proteins to generate models of helical fiber assemblies. Each two-component scaffold was initially treated as a single-component system, and only those with interfacial regions spanning multiple components were retained for further analysis. Design trajectories were filtered using the following criteria: a Rosetta energy difference greater than −15.0 REU between the polymeric (bound) and monomeric (unbound) states, an interface surface area exceeding 700 Å^2, a shape complementarity score above 0.62, and fewer than five unsatisfied polar residues. Designs meeting these thresholds were manually refined by reverting non-essential mutations to their native residues. The highest-scoring design from each configuration was selected for experimental validation. The complete amino acid sequences of all selected designs are provided in the Section S1 (Supporting Information).

Protein Expression and Purification: Gene sequences were codon-optimized for E. coli expression and synthesized commercially (Genscript and IDT). The constructs—either bicistronic or tricistronic—were inserted into pET29b(+) plasmids using NdeI and XhoI restriction sites. (Bicistronic means component A and B are encoded and expressed in the same plasmid; each component has it leading ribosome binding site so they can be co-expressed in cells.) When spatially feasible, GFP tags were attached to either the N- or C-terminus to facilitate visualization. In each construct, a single component was engineered to include a His_6 tag to allow purification through immobilized metal affinity chromatography (IMAC).

The plasmids were introduced into BL21(DE3)* competent E. coli cells and cultured in Terrific Broth (50 mL) supplemented with 200 mg L^{-1} kanamycin[54]. Protein expression was induced by the Studier autoinduction protocol and maintained at 37 °C for 24 h. Following the expression, cells were collected by centrifugation, resuspended in Tris-buffered saline (TBS), and lysed using Bugbuster reagent. After clarification by centrifugation, the soluble lysate was loaded onto Ni-NTA Superflow resin for IMAC purification. The resin was washed with ten column volumes of buffer containing 40 mM imidazole and 500 mM NaCl, and bound proteins were subsequently eluted with buffer containing 400 mM imidazole and 75 mM NaCl. Protein purity was examined by SDS-PAGE, and fractions containing bands at the expected molecular weight were selected for electron microscopy (EM) screening. For extended analyses, selected constructs were scaled up to 0.5 L cultures, expressed under identical conditions for 24 h at 37 °C, and lysed by microfluidization prior to purification using the same IMAC procedure.

Protein Assembly: Component A (140 µM, 50 µL) and Component B (140 µM, 50 µL) were mixed in a cold room (4 °C) and gently agitated on a rotator to facilitate assembly. At designated time points, 2 µL of the assembled solution was withdrawn and diluted to 1 µM in a 1 M KCl buffer to promote protein fiber deposition on the substrate for liquid AFM measurements. AFM imaging was conducted at 0, 10, 48, 72, and 90 h, and the results are presented in Figure 3.

Deposition of Protein Fibers: The assembled solution was diluted to 1 µM in KCl buffer of varying concentrations. A 100 µL droplet was placed onto freshly cleaved mica and incubated for 1 h to allow protein fibers to deposit on the surface. Afterward, in situ AFM measurements were performed with the solution still present to record the deposition results.

Liquid AFM Characterization: AFM imaging was performed in liquid at 25 °C using AC tapping mode on a Cypher ES instrument (Asylum Research). A Nanoworld probe (k = 0.15 N m^{-1}, f = 1200 kHz) was operated at a drive frequency of ≈500 kHz with a scanning rate of 1.5 Hz (512 lines per image). The AFM probe should be cleaned by UV-Ozone to remove potential contamination. The amplitude setpoint was adjusted to maintain surface topography. Samples were prepared by depositing a 70–100 µL droplet of 1 µM protein solution onto freshly cleaved mica. Data were processed and analyzed using Gwyddion software. When scanning an ellipse, the AFM tip artificially broadens the measured. The true width (W_{-true}) is related to the measured diameter (W_{ex}) by the simplified geometric approximation equation: $W_{-true} = W_{-ex}-(h_{-ex}-\delta_{-h}-2r)\tan\theta-2r$,[55] where h_{ex} is the experimentally measured height, W_{-ex} is the experimentally measured width, W_{-true} is the actual width of the tested fiber, δ_{-h} is the eliminated height of the ellipse, which is set to zero in the equation, r is the tip radius, θ is the effective tip angle. The values of r and θ are determined by the tip manufacturer: USC-F1.2-k0.15 tip: r = 10 nm, θ = 22°. Thus, the lateral broadening (Δx) introduced by the tip can be estimated as: $\Delta_{-}x = (h_{-ex}-\delta_{-h}-2r)\tan\theta+2r$, h_{-ex} ranged from 10–21 nm, the calculated lateral broadening is less than 13 nm, corresponding to an error of <18% in the measured helical pitch (≈70 nm). KCl and NaCl were purchased from Sigma–Aldrich, and dissolved into a certain concentration (0–3M). Muscovite mica substrate and HOPG were acquired from Ted Pella Inc and synthetic fluorophlogopite mica was acquired from MTI.

CryoEM Characterization: Cryo-TEM imaging was conducted on a JEOL GrandARM-300F microscope equipped with a Gatan OneView IS camera. Lacey carbon film Cu TEM grids were glow-discharged for 25 s at 15 mA using a PELCO easiGlow system prior to vitrification. A 3 µL aliquot of the reaction solution was applied to each grid, blotted for 4 s, and plunge-frozen in liquid ethane using an FEI Vitrobot Mark III. Images were acquired at a defocus range of −1—2 µm, with a total accumulated electron dose of less than ≈4 e$^-$ Å^{-2}.

Fast Force Mapping Mode: Fast Force Mapping AFM measurements were performed in amplitude-modulated mode on an Asylum Research Cypher Video-Rate Scanning (VRS) instrument, following established protocols[30,42,43]. Each force curve in the map was obtained from a complete cantilever approach–retract cycle, during which phase shift, amplitude, and deflection signals were recorded. ArrowUHFAuD probes (k = 3–6 N m^{-1}, f = 0.35–0.50 MHz) were used. The cantilever was driven photothermally at resonance using Asylum BlueDrive laser technology, with drive amplitudes in bulk solution maintained below 0.3 nm.

Supporting Information

Supporting Information is available from the Wiley Online Library or from the author.

Acknowledgements

AFM analyses were performed at Pacific Northwest National Laboratory (PNNL) with support from the US Department of Energy (DOE), Office of Science (SC), Office of Basic Energy Sciences (BES) through the Energy Frontier Research Center, the Center the Science of Synthesis Across Scales (CSSAS), under FWP 72448. Protein design and synthesis were performed at the Institute for Protein Design, University of Washington with support from the Howard Hughes Medical Institute (H.S. and D.B.), The Audacious Project (H.S. and D.B.), and the Defense Advanced Research Projects Agency Biostasis HR001118S0034 (H.S.). PNNL is a multiprogram national laboratory operated for DOE by Battelle under contract number DE-AC05–76RL01830.

Conflict of Interest

The authors declare no conflict of interest.

Data Availability Statement

The data that support the findings of this study are available in the supplementary material of this article.

Keywords

adsorption, AFM, de novo protein, interface, orientation

Received: August 9, 2025
Revised: October 24, 2025
Published online:

[1] D. Grafahrend, K.-H. Heffels, M. V. Beer, P. Gasteier, M. Möller, G. Boehm, P. D. Dalton, J. Groll, *Nat. Mater.* **2011**, *10*, 67.
[2] A. Hasan, S. K. Pattanayek, L. M. Pandey, *ACS Biomater. Sci. Eng.* **2018**, *4*, 3224.
[3] I. Firkowska-Boden, X. Zhang, K. D. Jandt, *Adv. Healthcare Mater.* **2018**, *7*, 1700995.
[4] M. Rabe, D. Verdes, S. Seeger, *Adv. Colloid Interface Sci.* **2011**, *162*, 87.
[5] K. Wang, C. Zhou, Y. Hong, X. Zhang, *Interface focus.* **2012**, *2*, 259.
[6] E. Ostuni, R. G. Chapman, R. E. Holmlin, S. Takayama, G. M. Whitesides, *Langmuir* **2001**, *17*, 5605.
[7] S. Roy, P. A. Covert, W. R. FitzGerald, D. K. Hore, *Chem. Rev.* **2014**, *114*, 8388.
[8] M. Kastantin, B. B. Langdon, D. K. Schwartz, *Adv. Colloid Interface Sci.* **2014**, *207*, 240.
[9] M. Veiseh, M. H. Zareie, M. Zhang, *Langmuir* **2002**, *18*, 6671.
[10] C. Stewart, B. Akhavan, S. G. Wise, M. M. Bilek, *Prog. Mater. Sci.* **2019**, *106*, 100588.
[11] H. Chen, L. Yuan, W. Song, Z. Wu, D. Li, *Prog. Polym. Sci.* **2008**, *33*, 1059.
[12] X. Su, J. Hübner, M. J. Kauke, L. Dalbosco, J. Thomas, C. C. Gonzalez, E. Zhu, M. Franzreb, T. F. Jamison, T. A. Hatton, *Chem. Mater.* **2017**, *29*, 5702.
[13] C. Shi, M. Zorman, X. Zhao, M. B. Salmeron, J. Pfaendtner, X. Y. Liu, S. Zhang, J. J. De Yoreo, *Sci. Adv.* **2024**, *10*, ado4142.
[14] S. Zhang, R. Sadre, B. A. Legg, H. Pyles, T. Perciano, E. W. Bethel, D. Baker, O. Rübel, J. J. De Yoreo, *Proc. Natl. Acad. Sci. USA* **2022**, *119*, 2020242119.
[15] S. Zhang, R. G. Alberstein, J. J. De Yoreo, F. A. Tezcan, *Nat. Commun.* **2020**, *11*, 3770.
[16] S. Zhang, J. Chen, J. Liu, H. Pyles, D. Baker, C. L. Chen, J. J. De Yoreo, *Adv. Mater.* **2021**, *33*, 1905784.
[17] H. Pyles, S. Zhang, J. J. De Yoreo, D. Baker, *Nature* **2019**, *571*, 251.
[18] I. Levental, E. Lyman, *Nat. Rev. Mol. Cell Biol.* **2023**, *24*, 107.
[19] C. Fu, Z. Wang, X. Zhou, B. Hu, C. Li, P. Yang, *Chem. Soc. Rev.* **2024**.
[20] J. Chen, E. Zhu, J. Liu, S. Zhang, Z. Lin, X. Duan, H. Heinz, Y. Huang, J. J. De Yoreo, *Science* **2018**, *362*, 1135.
[21] F. Teng, H. Zhang, D. Nykypanchuk, R. Li, L. Yang, N. Tiwale, Z. Xi, M. Liu, M. He, S. Zhang, *Nat. Commun.* **2025**, *16*, 3238.
[22] C. L. Brown, I. A. Aksay, D. A. Saville, M. H. Hecht, *J. Am. Chem. Soc.* **2002**, *124*, 6846.
[23] K. Kikuchi, T. Fukuyama, T. Uchihashi, T. Furuta, Y. T. Maeda, T. Ueno, *Small* **2022**, *18*, 2106401.
[24] G. G. Ferenczy, Ü. Murvai, L. Fülöp, M. Kellermayer, *Int. J. Mol. Sci.* **2024**, *25*, 10460.
[25] L. Hamon, D. Panda, P. Savarin, V. Joshi, J. Bernhard, E. Mucher, A. Mechulam, P. A. Curmi, D. Pastré, *Langmuir* **2009**, *25*, 3331.
[26] X. Zhou, Y. Zhang, F. Zhang, S. Pillai, J. Liu, R. Li, B. Dai, B. Li, Y. Zhang, *Nanoscale* **2013**, *5*, 4816.
[27] Z. Zhai, S. Y. Schmid, Z. Lin, S. Zhang, F. Jiao, *Aggregate* **2024**, *5*, 604.
[28] S. V. Kalinin, S. Zhang, M. Valleti, H. Pyles, D. Baker, J. J. De Yoreo, M. Ziatdinov, *ACS Nano* **2021**, *15*, 6471.
[29] J. L. Prelesnik, R. G. Alberstein, S. Zhang, H. Pyles, D. Baker, J. Pfaendtner, J. J. De Yoreo, F. A. Tezcan, R. C. Remsing, C. J. Mundy, *Proc. Natl. Acad. Sci. USA* **2021**, *118*, 2025121118.
[30] R. G. Alberstein, J. L. Prelesnik, E. Nakouzi, S. Zhang, J. J. De Yoreo, J. Pfaendtner, F. A. Tezcan, C. J. Mundy, *J. Phys. Chem. Lett.* **2022**, *14*, 80.
[31] H. Shen, E. M. Lynch, N. Jameson, J. Decarreau, C. Shi, Z. Chen, W. Sheffler, M. Xu, J. J. De Yoreo, J. G. Zalatan, *bioRxiv* **2025**, 2025.
[32] C. Shi, A. Y. Heble, S. Zhang, *Mater. Today Phys.* **2024**, 101429.
[33] S. Y. Schmid, K. Lachowski, H. T. Chiang, L. Pozzo, J. De Yoreo, S. Zhang, *Angew. Chem., Int. Ed.* **2023**, *62*, 202309725.
[34] J. W. Gibbs, *On the equilibrium of heterogeneous substances*, Tuttle, Morehouse & Taylor, New Haven, CT, USA **1874**.
[35] D. Kashchiev, *J. Chem. Phys.* **2003**, *118*, 1837.
[36] X. Ma, S. Zhang, F. Jiao, C. J. Newcomb, Y. Zhang, A. Prakash, Z. Liao, M. D. Baer, C. J. Mundy, J. Pfaendtner, *Nat. Mater.* **2017**, *16*, 767.
[37] S. Chung, S.-H. Shin, C. R. Bertozzi, J. J. De Yoreo, *Proc. Natl. Acad. Sci. USA* **2010**, *107*, 16536.
[38] P. G. Vekilov, *Nanoscale* **2010**, *2*, 2346.
[39] W. Ostwald, *Z. Phys. Chem.* **1897**, *22*, 289.
[40] T. Threlfall, *Org. Process Res. Dev.* **2003**, *7*, 1017.
[41] T. Fukuma, R. Garcia, *ACS Nano* **2018**, *12*, 11785.
[42] E. Nakouzi, A. G. Stack, S. Kerisit, B. A. Legg, C. J. Mundy, G. K. Schenter, J. Chun, J. J. De Yoreo, *J. Phys. Chem. C* **2020**, *125*, 1282.
[43] E. Nakouzi, S. Kerisit, B. A. Legg, S. Yadav, D. Li, A. G. Stack, C. J. Mundy, J. Chun, G. K. Schenter, J. J. De Yoreo, *J. Phys. Chem. C* **2023**, *127*, 2741.
[44] E. Nakouzi, S. N. Kerisit, J. Heo, B. A. Legg, M. Sassi, P. Simonnin, K. M. Rosso, *J. Phys. Chem. C* **2025**, *129*, 7550.
[45] E. Radoslovich, *Acta Crystallogr.* **1960**, *13*, 919.
[46] A. Tuladhar, Z. A. Chase, M. D. Baer, B. A. Legg, J. Tao, S. Zhang, A. D. Winkelman, Z. Wang, C. J. Mundy, J. J. De Yoreo, *J. Am. Chem. Soc.* **2019**, *141*, 2135.
[47] D. M. Arvelo, C. Garcia-Sacristan, E. Chacón, P. Tarazona, R. Garcia, *J. Chem. Phys.* **2024**, *160*, 164714.
[48] S. R. van Lin, K. K. Grotz, I. Siretanu, N. Schwierz, F. Mugele, *Langmuir* **2019**, *35*, 5737.
[49] A. Koishi, S. S. Lee, P. Fenter, A. Fernandez-Martinez, I. C. Bourg, *J. Phys. Chem. C* **2022**, *126*, 16447.
[50] S. Adapa, D. R. Swamy, S. Kancharla, S. Pradhan, A. Malani, *Langmuir* **2018**, *34*, 14472.
[51] B. Narayanan, G. H. Gilmer, J. Tao, J. J. De Yoreo, C. V. Ciobanu, *Langmuir* **2014**, *30*, 1343.
[52] C. Garcia-Sacristan, V. G. Gisbert, K. Klein, A. Šaric´, R. Garcia, *ACS Nano* **2024**, *18*, 18485.
[53] H. Shen, J. A. Fallas, E. Lynch, W. Sheffler, B. Parry, N. Jannetty, J. Decarreau, M. Wagenbach, J. J. Vicente, J. Chen, *Science* **2018**, *362*, 705.
[54] F. W. Studier, *Protein Expr. Purif.* **2005**, *41*, 207.
[55] C. Shi, Y. Bae, M. Zhang, J. J. De Yoreo, *Adv. Mater.* **2025**, 2501096.